

Modulating Anisotropic Magnetism of Layered CuCrP_2S_6 Single Crystal via Selenium Substitution

I. S. Eid^{1,2} and Li Song^{1,*}

¹National Synchrotron Radiation Laboratory, University of Science and Technology of China, Hefei, Anhui 230029, China

²Department of Physics, Faculty of Science, Benha University, Benha 13518, Egypt

*E-mail: song2012@ustc.edu.cn

ABSTRACT

As one of typical layered structures, antiferromagnetic CuCrP_2S_6 single crystal has high potential for magnetoelectric devices and spintronic multi-terminal chips due to its unique magnetic anisotropy. However, to tune the anisotropic magnetism is still challenge. Herein, high quality single crystals of $\text{CuCrP}_2(\text{S}_{1-x}\text{Se}_x)_6$ (where $X=0, 0.02, 0.05, 0.1, \text{ and } 0.2$) were grown via chemical vapor transport route, and the effect of selenium substitutions on the magnetic anisotropies in CuCrP_2S_6 were systematically investigated. The structural characterizations revealed that the $\text{CuCrP}_2(\text{S}_{1-x}\text{Se}_x)_6$ single crystals could remain the pristine monoclinic crystal phase with Se uniform dispersion in whole CuCrP_2S_6 . With Se substitution, the oxide states of P and S elements exhibited increased. The magnetic anisotropic results measured in normal and parallel directions between the crystallographic plane (**ab**) and the applied magnetic field (**H**) showed that the Néel temperatures (T_N) and temperatures at maximum magnetic susceptibilities (T_{Max}) in **H \perp ab** and **H \parallel ab** decreased with increasing the selenium doping amounts in $\text{CuCrP}_2(\text{S}_{1-x}\text{Se}_x)_6$ single crystals. Notably, their anisotropic behavior in paramagnetic phase tends to be isotropic with increasing selenium concentrations. Moreover, the transitions of the spin flop, which appear only in case of **H \perp ab**, was greatly suppressed with increasing the selenium concentrations in $\text{CuCrP}_2(\text{S}_{1-x}\text{Se}_x)_6$ until disappearing at $X=0.1$ and 0.2 . The spin polarized density functional theory calculations further confirmed that the asymmetry between spin up and spin down states in CuCrP_2S_6 could be highly modulated via Se substitution, resulting in the tunable anisotropic magnetism of hybridized $\text{CuCrP}_2(\text{S}_{1-x}\text{Se}_x)_6$. Our findings make these materials to be more interesting in spintronic applications.

KEYWORDS: Transition Metal Phosphorous Trichalcogenides, $\text{CuCrP}_2(\text{S}_{1-x}\text{Se}_x)_6$ Single Crystals, Elemental Substitution, Magnetic Anisotropy, Density Functional Theory Calculations

I. INTRODUCTION

Since the successful fabrication of a graphene monolayer, two-dimensional layered materials have occupied a remarkable attention due to their unique electronic, optical, and magnetic properties [1, 2]. Among them, Transition Metal Phosphorous Trichalcogenides ($M_2P_2X_6$; $X=S$ and Se) with untraditional magnetic and electronic properties are more promising for many specific applications [3-9]. Generally, $M_2P_2X_6$ compounds are structurally composed of van der Waals alternating stacking of a few or several layers dependent of their thickness [10, 11]. In principle, such $M_2P_2X_6$ can be geometrically formed in a monoclinic crystal structure with various magnetic properties based on the electronic occupations in 3d of transition metals [12].

Recently, $CuCrP_2S_6$ as one of typical $M_2P_2X_6$ materials has attracted many efforts because of the presence of both the intrinsic antiferromagnetic and antiferroelectric features in its structure [13-15]. In principle, $CuCrP_2S_6$ is crystallized in a monoclinic unit cell with alternating periodic arrangements of Cu and Cr atoms through its honeycomb sublattice, in which the antiferroelectricity generated by Cu and the antiferromagnetism generated by Cr [16, 17]. Experimentally, Colombet et al. [18] found that $CuCrP_2S_6$ behaved as an antiferromagnetic material below Néel temperature (T_N)=30 K. Selter et al. [19] further reported that the four stacking layers of $CuCrP_2S_6$ showed the antiferromagnetic characteristics below similar temperature as well as a positive value of Curie-Weiss temperature. More interestingly, $CuCrP_2S_6$ can also exhibit magnetic anisotropies in its intrinsic antiferromagnetic phase. Wang et al. [20] found that the antiferromagnetism in $CuCrP_2S_6$ was displayed below $T_N=32$ K with considerable magnetic anisotropies through the crystallographic directions. Additionally, they reported the coexistence of spin flop transitions which illustrated a high anisotropy with changing the crystallographic directions.

In fact, such intrinsic magnetic properties of $M_2P_2X_6$ materials can be tuned by applying an external pressure or chemical substitutions [21, 22], subsequently exhibiting various anisotropies [23, 24]. For example, parent systems of $Ni_2P_2S_6$ and $Fe_2P_2S_6$ showed different magnetic anisotropies in comparison with $(Fe_{1-x}Ni_x)_2P_2S_6$ as an intermediate system between them [25]. Besides, the effect of the chemical substitutions between Ni and Mn ions was studied on the magnetic anisotropic characteristics in $(Mn_{1-x}Ni_x)_2P_2S_6$ layered single crystals in comparison with their parent counterparts ($Mn_2P_2S_6$ and $Ni_2P_2S_6$) [21, 26]. Abraham *et al.* [27] investigated the magnetic anisotropy in mixed transition metallic cations system of $MnNiP_2S_6$ which was compared

with $\text{Mn}_2\text{P}_2\text{S}_6$. Moreover, $\text{CuCr}_{1-x}\text{In}_x\text{P}_2\text{S}_6$ compound elucidated a modulation in its magnetic anisotropy via the substitution between Cr and In ions [28]. Recently, some evolutions of magnetic anisotropies in different $\text{M}_2\text{P}_2\text{X}_6$ systems have been investigated by the means of elemental substitutions [29, 30]. Therefore, it is highly desirable to develop a controllable approach to modulate the magnetism of $\text{M}_2\text{P}_2\text{X}_6$ for more applications.

Herein, we demonstrate a chemical vapor transport route to facile modulate the anisotropic magnetism of CuCrP_2S_6 via in-situ selenium substitution. Scanning electron microscopy (SEM) and energy dispersive X-ray spectroscopy (EDS) were used for morphological and compositional characterizations of the grown $\text{CuCrP}_2(\text{S}_{1-x}\text{Se}_x)_6$ single crystals. X-ray diffraction (XRD), high resolution transmission electron microscope (HRTEM), selected area electron diffraction (SAED) were employed to characterize their single crystallinity. The chemical bonding states in the crystals were studied by X-ray photoelectron spectroscopy (XPS). The experimental magnetic measurements revealed that the anisotropic antiferromagnetism of $\text{CuCrP}_2(\text{S}_{1-x}\text{Se}_x)_6$ can highly modulated by Se doping amounts. Moreover, spin polarized density functional theory (DFT) calculations have been performed to study the effect of Se substitutions on the magnetic properties of the parent compound CuCrP_2S_6 .

II. RESEARCH METHODOLOGY

1. EXPERIMENTAL METHODOLOGY

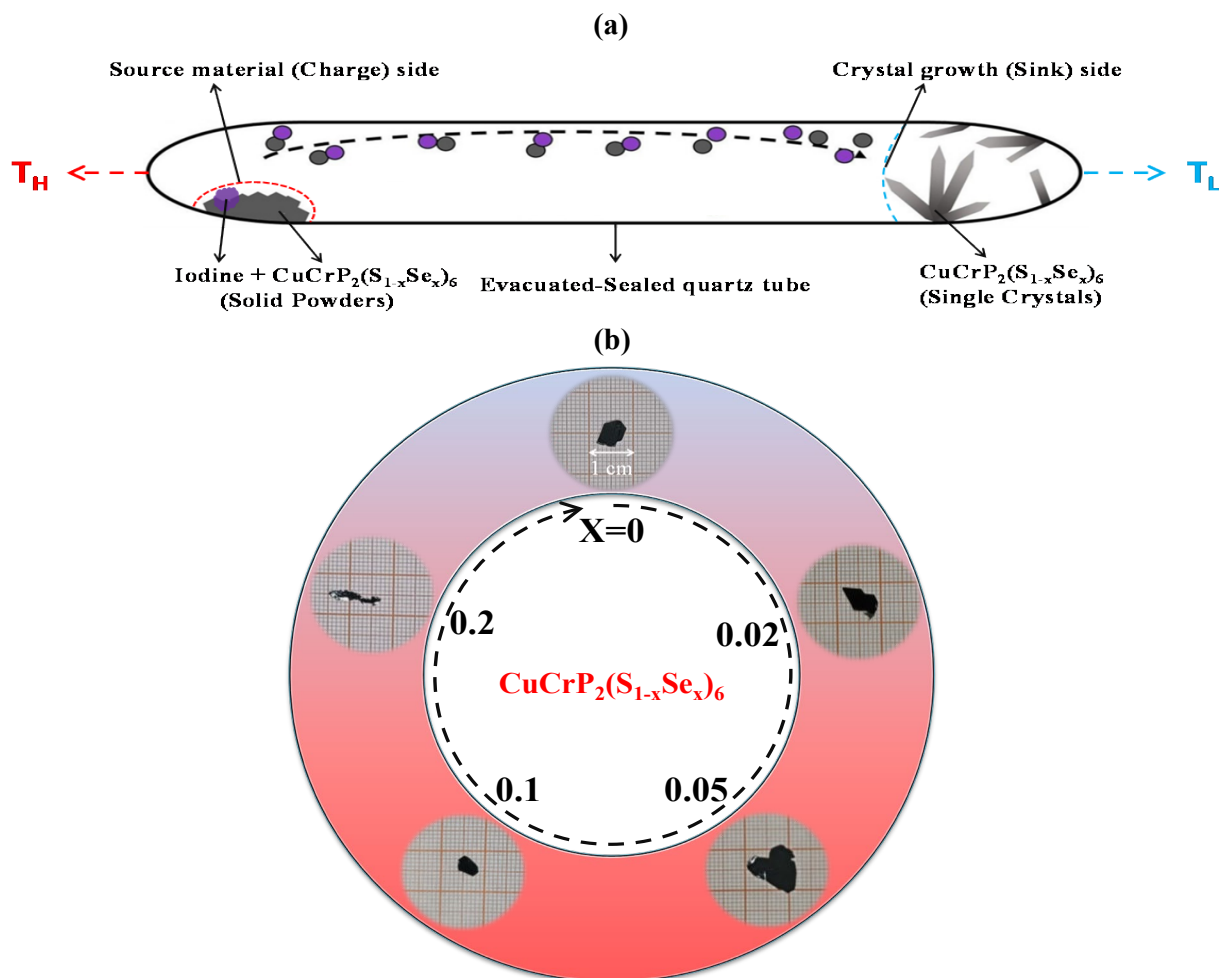


Figure 1: (a) Schematic illustration of the tube during the CVT reaction for synthesizing $\text{CuCrP}_2(\text{S}_{1-x}\text{Se}_x)_6$ single crystals, and (b) Optical images of the grown $\text{CuCrP}_2(\text{S}_{1-x}\text{Se}_x)_6$ crystals for ($X=0, 0.02, 0.05, 0.1, \text{ and } 0.2$).

High qualities of $\text{CuCrP}_2(\text{S}_{1-x}\text{Se}_x)_6$ single crystals ($X=0, 0.02, 0.05, 0.1, \text{ and } 0.2$) were grown by chemical vapor transport (CVT) technique. The solid powders of the elements in the stoichiometric molar proportions of Cu, Cr, P, S, and Se were mixed together as a source material with iodine (~30-31 mg) as a transport agent and were sealed in a 15 cm long evacuated sealed quartz tube with 1 cm inner diameter as shown in **Figure 1(a)**. This tube was transported horizontally into a two-zone furnace in which the two zones were defined as a source (charge) side with a higher temperature (T_H) and sink (crystal growth) side with a lower temperature (T_L). The controlled temperature profile of the furnace was set up where the charge and sink sides were raised within 360 min from room temperature to 300 °C for satisfying the pre-reaction of P, S, and Se elements with the transition elements [25]. Then, after 1 day, the charge side temperature was set up at 690

°C while the sink side became at 620 °C. Finally, both sides were dewelled at these temperatures for 6 days (crystal growth phase) and then, the furnace was slowly cooled to the room temperature. The optical images of the grown crystals extracted from the tube, are demonstrated as shown in **Figure 1(b)**.

2. CALCULATION METHODS

DFT calculations with spin polarization effects were employed by using Vienna ab initio simulation package (VASP) [31]. The PBE functional was used to express the ion-electron interaction and generalized gradient approximation (GGA) [32] which were characterized by projector augmented wave (PAW) method [33, 34]. The energy cut off of a plane wave was set to 385 eV. Also, Gaussian smearing was set to equal 0.05 eV. The energy convergence was considered in precision of 10^{-6} eV. All atoms were fully relaxed in the structure until the force became less than 0.01 eV/Å. In addition, the Brillouin zone was performed with a 6 x 3 x 3 Monkhorst-Pack of k-points scheme [35] for the geometrical optimization of the structures while it became 12 x 6 x 6 k-points for density of state (DOS) calculations.

III. RESULTS AND DISCUSSION

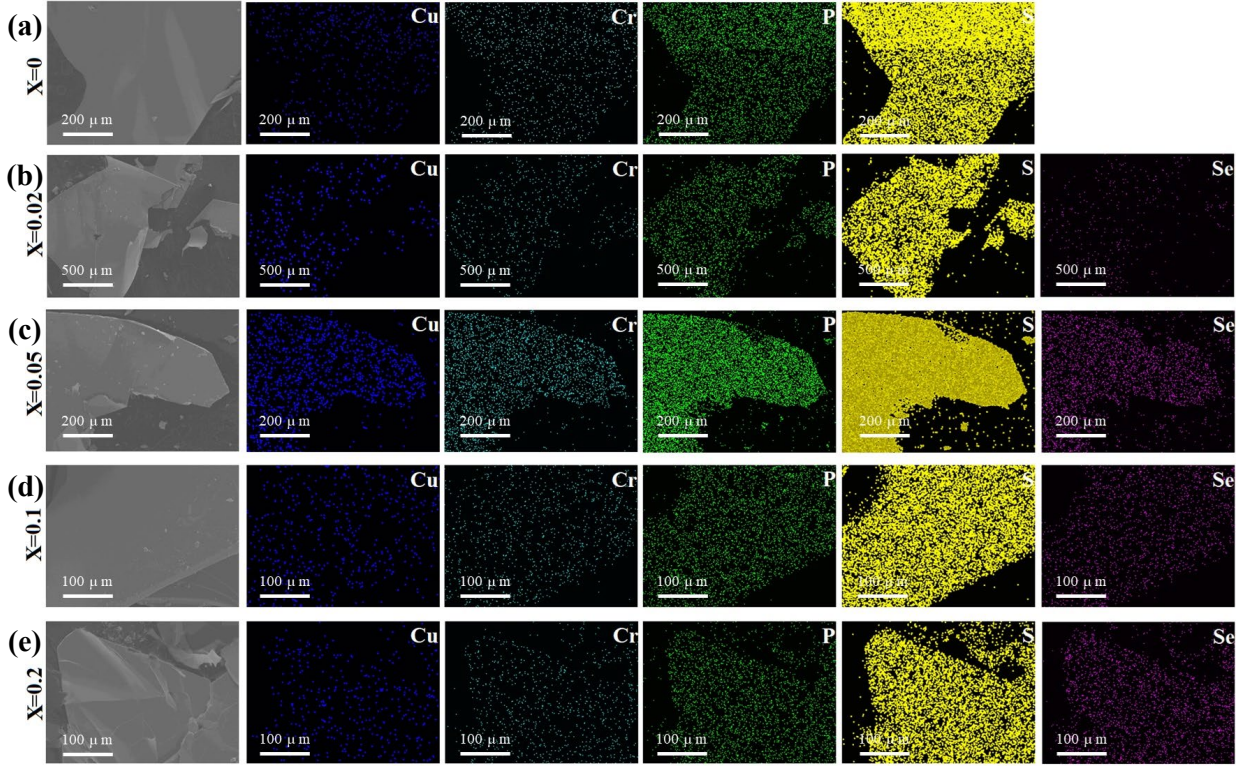


Figure 2: SEM images and their corresponding EDS elemental mappings of the cleaved grown CuCrP₂(S_{1-x}Se_x)₆ crystals for (X=0 (a), 0.02 (b), 0.05 (c), 0.1 (d), and 0.2 (e)).

The layered morphological nature of all cleaved grown CuCrP₂(S_{1-x}Se_x)₆ crystals for (X=0 (a), 0.02 (b), 0.05 (c), 0.1 (d), and 0.2 (e)) is demonstrated according to SEM images, as shown in **Figure 2**. Their corresponding EDS measurements illustrate a homogenous distribution of all elements through the whole crystalline surface. Besides, the compositional analysis of the atomic percentages of all elements inside the crystalline surfaces is recorded, as seen in **Table 1**. It is observed that there is an acceptable deviation in the atomic percentage values of the elements between the experimentally used precursor values and measured EDS values. This is due to several parameters associated with CVT reactions, such as the duration and the temperature of the crystal growth, the transport agent type and the temperature gradient between the source and sink sides [36].

Table 1: Atomic percentages of elements in CuCrP₂(S_{1-x}Se_x)₆ crystals.

X _{Se} in CuCrP ₂ (S _{1-x} Se _x) ₆	Cu (At %)	Cr (At %)	P (At %)	S (At %)	Se (At %)
0	11.25	11.81	18.09	58.86	0
0.02	11.13	12.77	18.23	56.97	0.9
0.05	11.84	11.31	18.85	55.60	2.41

0.1	12.83	12.24	17.60	52.91	4.43
0.2	11.48	11.77	18.20	50.42	8.13

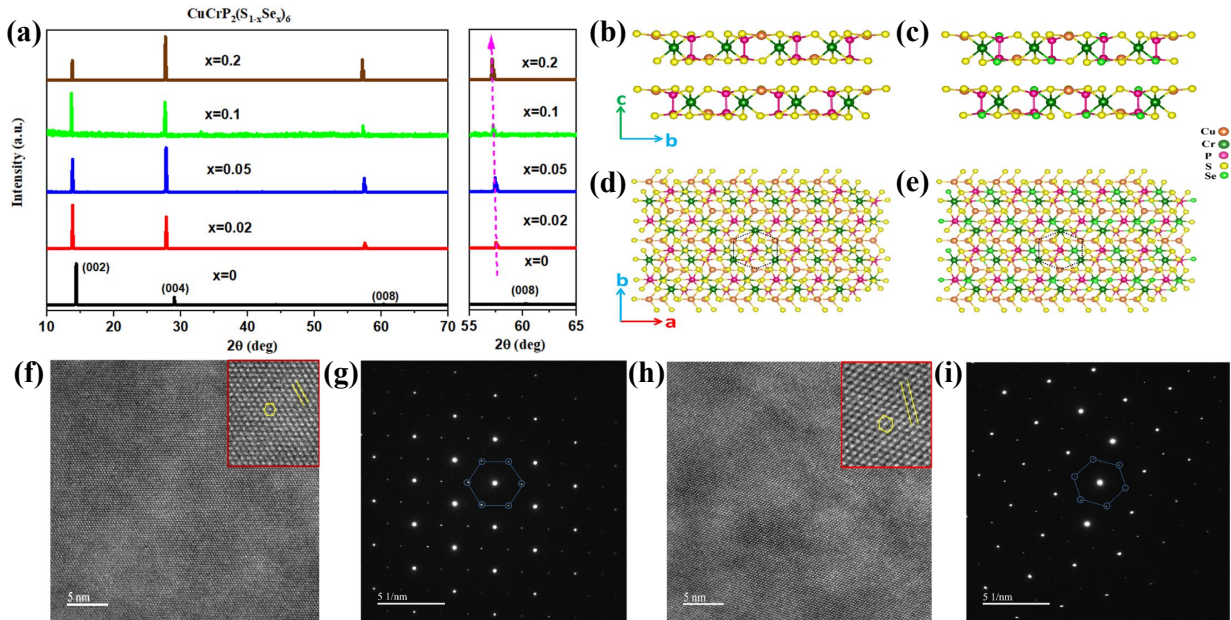


Figure 3: Crystal Structural Characterization. (a) XRD pattern of $\text{CuCrP}_2(\text{S}_{1-x}\text{Se}_x)_6$ single crystals ($X=0, 0.02, 0.05, 0.1, 0.2$). Atomic structure models of CuCrP_2S_6 ($X=0$) and $\text{CuCrP}_2\text{S}_{4.8}\text{Se}_{1.2}$ ($X=0.2$) from side view (b, c), as well as top view (d, e). HRTEM image of CuCrP_2S_6 ($X=0$) (f) and $\text{CuCrP}_2\text{S}_{4.8}\text{Se}_{1.2}$ ($X=0.2$) (h), and their corresponding SAED patterns (g) and (i).

According to XRD patterns of $\text{CuCrP}_2(\text{S}_{1-x}\text{Se}_x)_6$ single crystals as shown in Figure 3(a), the diffraction peaks (002), (004), and (008) of pristine CuCrP_2S_6 have been indexed well in agreement with the literatures [15, 20, 37]. It can be observed that the undoped CuCrP_2S_6 has a monoclinic crystal phase with Pc space group [20]. In addition, it is clearly seen that these peaks have been shifted to lower Bragg's angles under selenium doping because the ionic radius of sulfur is smaller than that of selenium. Also, with increasing the Se substitution from $X = 0.02$ to $X = 0.2$, there is a monotonic gradual observable deviation of (008) peaks towards the lower Bragg's angles in agreement with literatures [29, 30]. The peaks shift to the lower Bragg's angles under Se doping indicates to the elongation occurred along (c) crystal axis due to the difference in ionic radii of S and Se. Figure 3 ((b)-(e)) represent the crystal structure visualizations of undoped CuCrP_2S_6 (side view (b) and top view (d)) and Se doped CuCrP_2S_6 for $X=0.2$ (side view (c) and top view (e)). In the atomic models, a regular alternating arrangement of Cu and Cr cations in hexagonal rings is

demonstrated through the whole structure for undoped and Se doped CuCrP_2S_6 crystals. In **Figure 3**, HRTEM images and their corresponding SAED patterns of pristine CuCrP_2S_6 ((**f**) and (**g**)) and Se doped CuCrP_2S_6 at $X=0.2$ ((**h**) and (**i**)) elucidate the layered morphological nature and the uniform atomic distribution with hexagonal shaped rings throughout the crystal structure without any clustering of Se dopant in agreement with the above SEM observations.

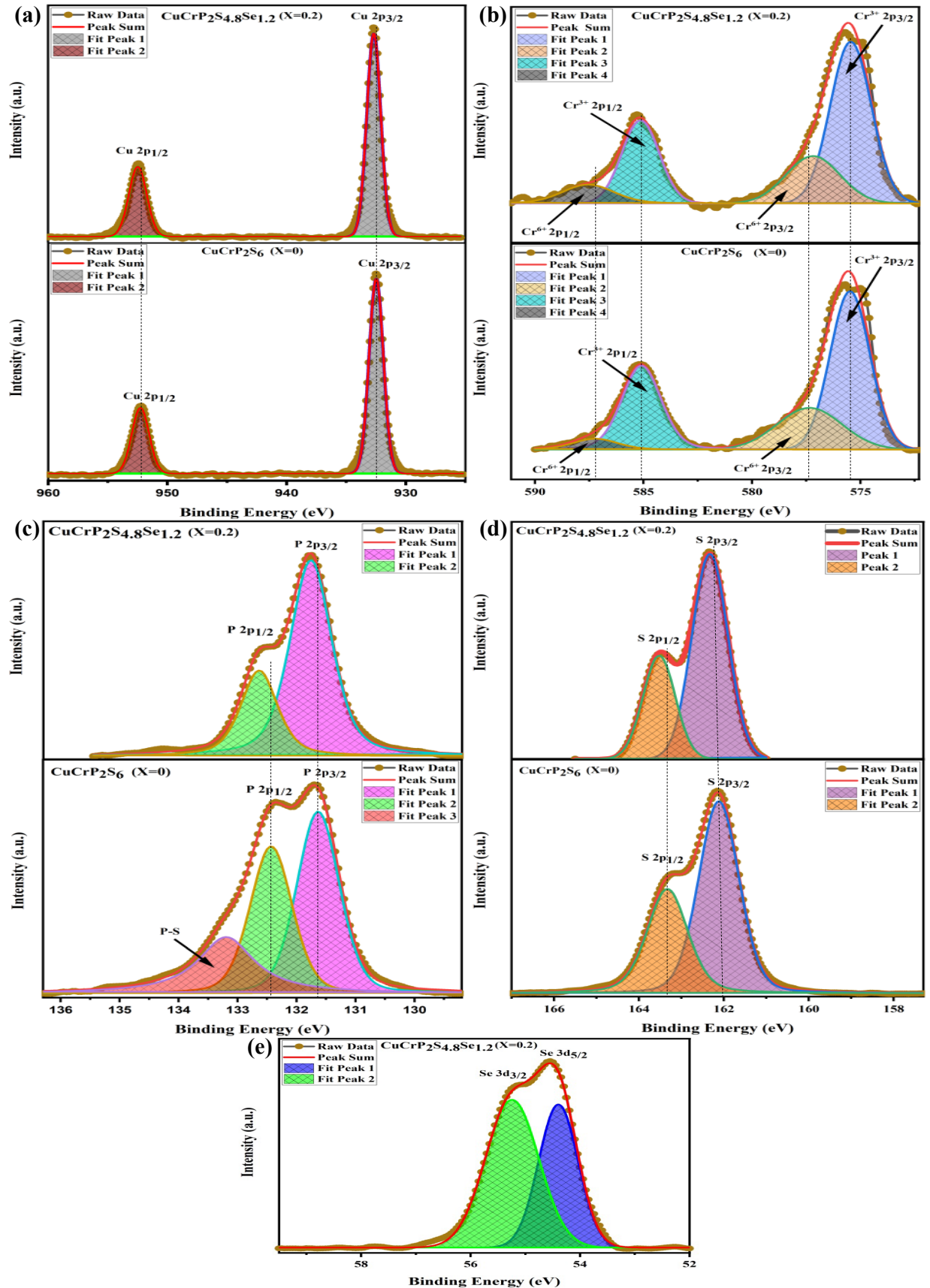


Figure 4: XPS spectra of (a) Cu 2p, (b) Cr 2p, (c) P 2p, (d) S 2p and (e) Se 3d of pure CuCrP₂S₆ and Se doped CuCrP₂S₆(CuCrP₂S_{4.8}Se_{1.2}).

For optimizing the evolution of chemical bonding states under the Se doping effect in CuCrP₂S₆, we employed XPS for characterizing CuCrP₂(S_{1-x}Se_x)₆ crystals for X=0 (pristine CuCrP₂S₆) and X=0.2 (CuCrP₂S_{4.8}Se_{1.2}). As shown in **Figure 4(a)**, we have observed that the Cu 2p peaks of doped and undoped CuCrP₂S₆ include the same two peaks assigned to Cu 2p_{1/2} and Cu 2p_{3/2}. The Cu 2p_{1/2} peak is detected at 952.27 eV and 952.47 eV, while Cu 2p_{3/2} peak is positioned at 932.49 eV and 932.68 eV for pristine CuCrP₂S₆ and Se doped CuCrP₂S₆, respectively. This indicates that Cu 2p peaks for doped CuCrP₂S₆ are slightly shifted to the higher binding energies compared to the same peaks in undoped CuCrP₂S₆. Also, **Figure 4(b)** shows that in doped and undoped CuCrP₂S₆, Cr 2p exhibited similar four peaks assigned as Cr³⁺ 2p_{1/2}, Cr³⁺ 2p_{3/2}, Cr⁶⁺ 2p_{1/2}, and Cr⁶⁺ 2p_{3/2}. For pristine CuCrP₂S₆, Cr³⁺ 2p_{1/2} and Cr³⁺ 2p_{3/2} are located at 585.10 eV and 575.48 eV, respectively. The two peaks are found at 585.14 eV and 575.45 eV for CuCrP₂S_{4.8}Se_{1.2}. It is clearly seen that there is no a considerable shift for these peaks in both doped and undoped CuCrP₂S₆. In addition, Cr⁶⁺ 2p_{1/2} peak is detected at 587.23 eV and 587.55 eV for undoped and doped CuCrP₂S₆, respectively, while Cr⁶⁺ 2p_{3/2} peak is seen at 577.35 eV and 577.19 eV for undoped and doped CuCrP₂S₆, respectively. It is further noticed that Cr⁶⁺ 2p_{1/2} peak in Se doped CuCrP₂S₆ is shifted to the higher binding energies compared to the pristine structure while Cr⁶⁺ 2p_{3/2} peak in doped CuCrP₂S₆ is very slightly shifted to the lower binding energies compared to the pristine CuCrP₂S₆. Moreover, as illustrated in **Figure 4(c)**, the P 2p peaks of pristine CuCrP₂S₆ are involved into three peaks assigned as P-S, P 2p_{1/2}, and P 2p_{3/2}. These peaks are respectively detected at 133.20 eV, 132.43 eV, and 131.64 eV in undoped CuCrP₂S₆. In comparison with pristine CuCrP₂S₆, there are only two peaks of P 2p in doped CuCrP₂S₆ named as P 2p_{1/2} and P 2p_{3/2} positioned at 132.64 eV and 131.76 eV, respectively. Comparison of both structures shows that the extra peak in the pristine structure refers to the formation of the chemical bonds on its crystalline surface between phosphorus and sulfur. Besides, it is demonstrated that P 2p_{1/2} and P 2p_{3/2} peaks for doped CuCrP₂S₆ are shifted to the higher binding energies compared with the same peaks in undoped CuCrP₂S₆ hence indicating that Se substitution results in donation of electrons to the pristine system resulting in increase in oxidation state. Also, **Figure 4(d)** illustrates the two peaks of S 2p (S 2p_{1/2} and S 2p_{3/2}) for undoped and doped CuCrP₂S₆. S 2p_{1/2} peak is detected at 163.33 eV and

163.52 eV while S 2p_{3/2} peak is localized at 162.12 eV and 162.33 eV for undoped and doped CuCrP₂S₆, respectively. It is shown that S 2p_{1/2} and S 2p_{3/2} peaks for doped CuCrP₂S₆ are shifted to higher binding energies compared with the similar peaks in the pristine CuCrP₂S₆ hence resulting in increase in oxidation state as well. Furthermore, as demonstrated in **Figure 4(e)**, Se 3d peaks in Se doped CuCrP₂S₆ include two peaks assigned as Se 3d_{3/2} and Se 3d_{5/2}. Se 3d_{3/2} and Se 3d_{5/2} peaks are located at 55.24 eV and 54.40 eV. All above XPS peaks have been indexed in accordance with the previous literatures [23, 38-42]. The observed displacements of Cu, Cr, P, and S peaks to the higher binding energy after Se doping show that selenium atoms have a large tendency to loss more electrons leading to a charge transfer to its neighbors [43].

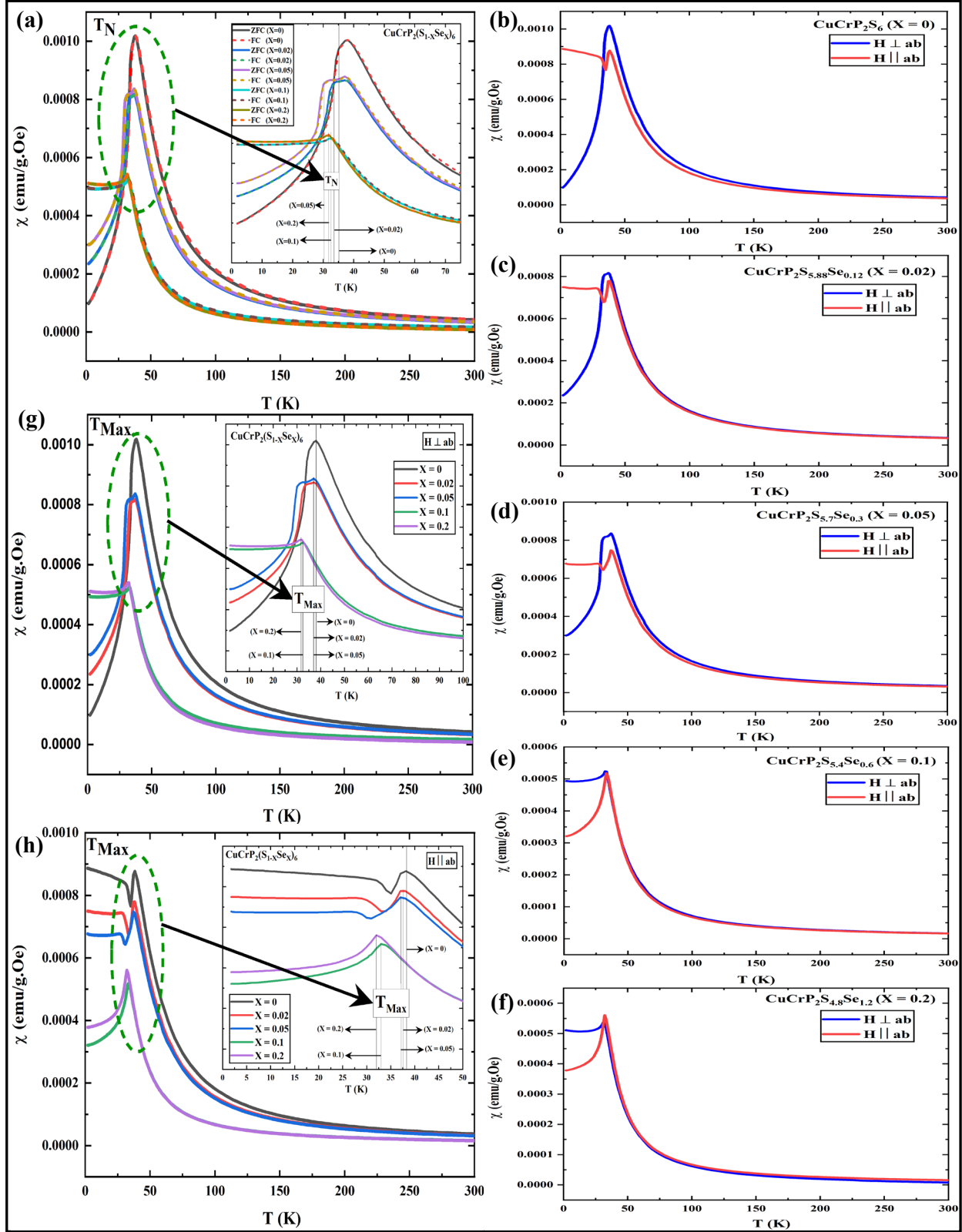


Figure 5: Magnetic susceptibility ($\chi(\text{emu/g.Oe})$) as a function of the temperature (T (K)) for an applied magnetic field of 1000 Oe (a) Zero Field Cooling (ZFC) and Non-Zero Field Cooling (FC) for $\text{CuCrP}_2(\text{S}_{1-x}\text{Se}_x)_6$ crystals. The inset in (a) represents a zoomed view of the Néel

temperature (T_N) positions. **(b)**, **(c)**, **(d)**, **(e)**, and **(f)** show the χ vs. T curves for $\text{CuCrP}_2(\text{S}_{1-x}\text{Se}_x)_6$ crystals at $X=0, 0.02, 0.05, 0.1,$ and 0.2 , respectively, in both normal and parallel directions of the applied magnetic field \mathbf{H} to the \mathbf{ab} crystal plane. **(g)** and **(h)** are χ vs. T curves in $\mathbf{H} \perp \mathbf{ab}$ and $\mathbf{H} \parallel \mathbf{ab}$, respectively, for $\text{CuCrP}_2(\text{S}_{1-x}\text{Se}_x)_6$ crystals. The insets in **(g)** and **(h)** indicate to the positions of the temperature at maximum magnetic susceptibility (T_{Max}).

Figure 5(a) demonstrates the magnetic susceptibility (χ) as a function of temperature (T) in both Zero Field Cooling (ZFC) and Non-Zero Field Cooling (FC) plotted at 1000 Oe of applied magnetic field (\mathbf{H}) to determine the Néel Temperature (T_N) of $\text{CuCrP}_2(\text{S}_{1-x}\text{Se}_x)_6$ crystals, where $X=0, 0.02, 0.05, 0.1,$ and 0.2 . It is clearly seen that with increasing the doping ratios of selenium in $\text{CuCrP}_2(\text{S}_{1-x}\text{Se}_x)_6$ structures, the values of T_N decrease in agreement with the literature [30], except at $X=0.05$ which has deviated from this behavior as illustrated in **Table 2**. Also, it can be observed that the values of the magnetic susceptibility have still unchanged in both ZFC and FC measurements. In addition, from **Figure 5(b)** to **Figure 5(f)**, an external magnetic field (\mathbf{H}) with intensity 1000 Oe was applied in the normal and parallel directions to the crystallographic plane \mathbf{ab} , respectively, for studying isotropic and anisotropic magnetic properties of $\text{CuCrP}_2(\text{S}_{1-x}\text{Se}_x)_6$ crystals. Moreover, the behavior of temperature-dependence magnetic susceptibility relations in case of $\mathbf{H} \perp \mathbf{ab}$ differs from that in case of $\mathbf{H} \parallel \mathbf{ab}$ confirming the existence of anisotropic characteristics in $\text{CuCrP}_2(\text{S}_{1-x}\text{Se}_x)_6$ structures. Besides, with increasing the selenium doping amounts, the anisotropic characteristics in the paramagnetic phase ($T > T_N$) tend to be semi-isotropic unlike the antiferromagnetic phase ($T_N > T$) in which the isotropic characteristics remain dominant. Furthermore, the antiferromagnetic profile for $\mathbf{H} \perp \mathbf{ab}$ is longer than that for $\mathbf{H} \parallel \mathbf{ab}$ in $\text{CuCrP}_2(\text{S}_{1-x}\text{Se}_x)_6$ crystals at $X=0, 0.02,$ and 0.05 on contrary to the case at $X=0.1$ and $X=0.2$. Compared to the length of antiferromagnetic profile in $\mathbf{H} \parallel \mathbf{ab}$, it is demonstrated that the length of antiferromagnetic path $\mathbf{H} \perp \mathbf{ab}$ decreases gradually with increasing the selenium doping in $\text{CuCrP}_2(\text{S}_{1-x}\text{Se}_x)_6$. Notably, the mismatching in isotropic and anisotropic properties between antiferromagnetic and paramagnetic phases has also been reported for other $\text{M}_2\text{P}_2\text{X}_6$ single crystals [44]. According to **Figures 5(g)** and **5(h)**, the temperatures at maximum magnetic susceptibility values (T_{Max}) in case of $\mathbf{H} \perp \mathbf{ab}$ measurements differ from those for $\mathbf{H} \parallel \mathbf{ab}$ measurements as recorded in **Table 2**. It is elucidated that T_{Max} for $\mathbf{H} \parallel \mathbf{ab}$ is higher than that for $\mathbf{H} \perp \mathbf{ab}$ except at $X=0.05$ where T_{Max} values are the same in both situations. Besides, we can easily observe that T_{Max} in both situations ($\mathbf{H} \perp \mathbf{ab}$ and $\mathbf{H} \parallel \mathbf{ab}$) decreases with the increase in the selenium doping of $\text{CuCrP}_2(\text{S}_{1-x}\text{Se}_x)_6$ crystals.

Table 2: Néel temperature (T_N) values and the temperature values at maximum magnetic susceptibilities (T_{Max}) in both $\mathbf{H} \perp \mathbf{ab}$ and $\mathbf{H} \parallel \mathbf{ab}$ for $\text{CuCrP}_2(\text{S}_{1-x}\text{Se}_x)_6$.

X_{Se} in $\text{CuCrP}_2(\text{S}_{1-x}\text{Se}_x)_6$	T_N (K)	T_{Max} (K) ($\mathbf{H} \perp \mathbf{ab}$)	T_{Max} (K) ($\mathbf{H} \parallel \mathbf{ab}$)
0	35.29	37.89	38.20
0.02	33.31	37	37.59
0.05	30.57	37	37
0.1	32.54	32.54	33.17
0.2	31.8	31.94	32.01

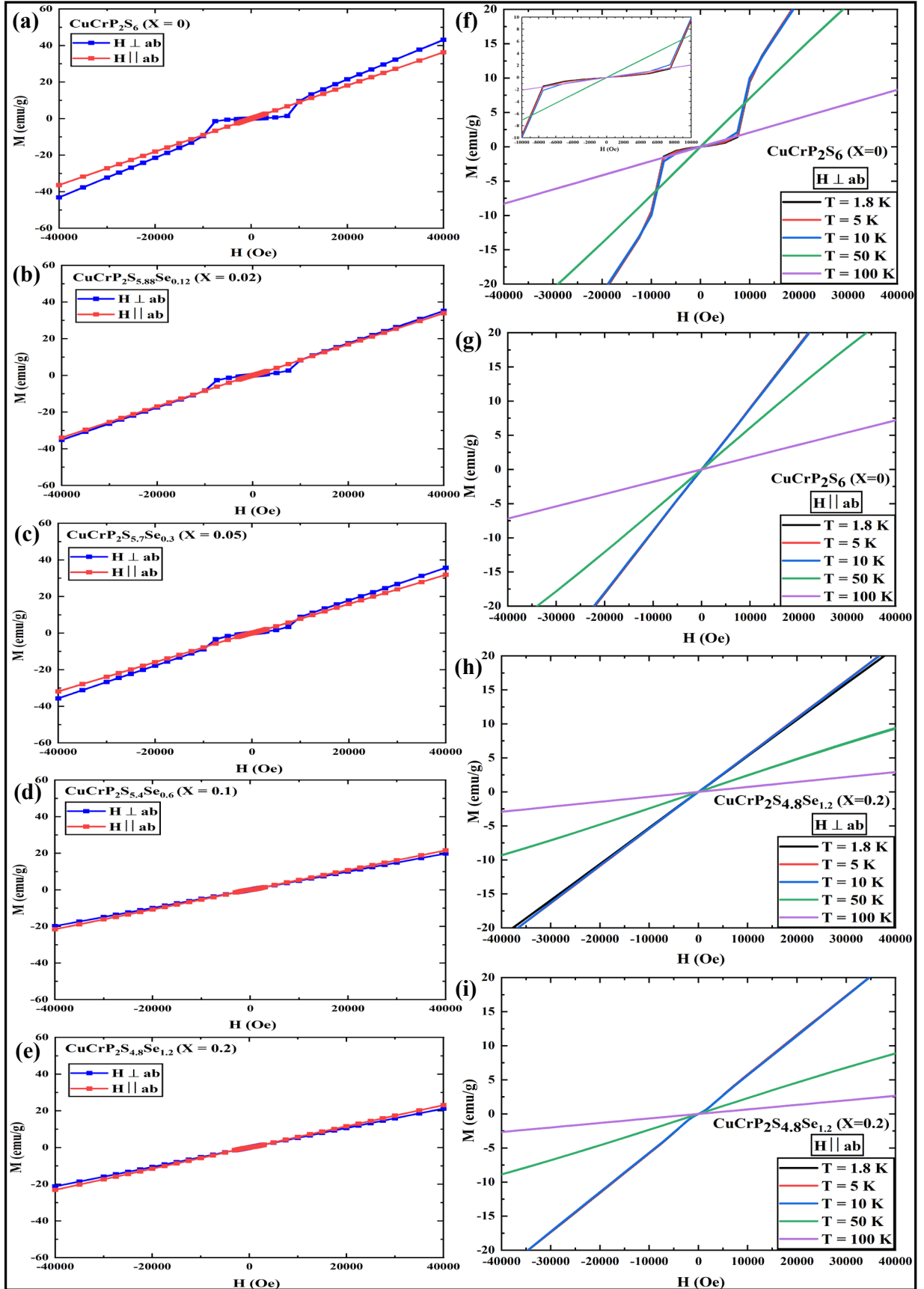


Figure 6: (a), (b), (c), (d), and (e) represent the hysteresis loops (\mathbf{M} vs. \mathbf{H}) at $T=1.8$ K of $\text{CuCrP}_2(\text{S}_{1-x}\text{Se}_x)_6$ crystals at $X=0, 0.02, 0.05, 0.1,$ and $0.2,$ respectively, in both $\mathbf{H} \perp \mathbf{ab}$ and $\mathbf{H} \parallel \mathbf{ab}$. (f) and (g) are \mathbf{M} vs. \mathbf{H} curves of CuCrP_2S_6 ($X=0$) for $\mathbf{H} \perp \mathbf{ab}$ and $\mathbf{H} \parallel \mathbf{ab}$, respectively, at different temperatures ($T=1.8$ K, 5 K, 10 K, 50 K, and 100 K). (h) and (i) indicate \mathbf{M} vs. \mathbf{H} curves of Se-doped CuCrP_2S_6 ($\text{CuCrP}_2\text{S}_{4.8}\text{Se}_{1.2}$ ($X=0.2$)) for $\mathbf{H} \perp \mathbf{ab}$ and $\mathbf{H} \parallel \mathbf{ab}$, respectively, at different temperatures ($T=1.8$ K, 5 K, 10 K, 50 K, and 100 K).

The relation between the magnetization (\mathbf{M}) and the applied magnetic field (\mathbf{H}) for $\text{CuCrP}_2(\text{S}_{1-x}\text{Se}_x)_6$ compounds has been demonstrated at $T=1.8$ K in **Figures 6(a)-(e)**. It is observed that a linear relation between \mathbf{M} and \mathbf{H} remains dominant in case of $\mathbf{H} \parallel \mathbf{ab}$ for all selenium doping amounts at $X=0$ (**Figure 6(a)**), $X=0.02$ (**Figure 6(b)**), $X=0.05$ (**Figure 6(c)**), $X=0.1$ (**Figure 6(d)**), and $X=0.2$ (**Figure 6(e)**). On the other hand, in case of $\mathbf{H} \perp \mathbf{ab}$, clear transitions of the spin flop appear for the parent compound CuCrP_2S_6 as shown in **Figure 6(a)** as well as for the doped compounds at $X=0.02$ (**Figure 6(b)**) and $X=0.05$ (**Figure 6(c)**) while these transitions are overlapped and disappeared for the doped compounds at $X=0.1$ (**Figure 6(d)**) and $X=0.2$ (**Figure 6(e)**). Moreover, from **Figure 6(a)** to **Figure 6(e)**, with increasing the selenium doping amounts, the spin flop is gradually suppressed and becomes more broadened and very weak. Similar phenomenon has been reported for $(\text{Mn}_{1-x}\text{Ni}_x)_2\text{P}_2\text{S}_6$ single crystals [21]. The occurred change in the anisotropic properties is essentially detected due to the interplay between the schemes of the crystal field effect and the anisotropy of the single-ion together with the spin-orbit coupling effects (SOC) [44]. Also, in other van der Waals crystals, such as transition-metal mixed halides [45] and $\text{Cu}_{2x}\text{Fe}_{1-x}\text{PS}_3$ [46], the magnetic anisotropic properties were observed and tuned based on the changes in the compositional elemental contents. Furthermore, the temperature-dependence evolution of the relation between \mathbf{M} and \mathbf{H} has been illustrated in **Figure 6(f)** to **Figure 6(i)**. **Figure 6(f)** shows that the spin flop transitions of the parent compound CuCrP_2S_6 in case of $\mathbf{H} \perp \mathbf{ab}$ appear only at $T=1.8$ K, $T=5$ K, and $T=10$ K while they disappear at $T=50$ K and $T=100$ K. Also, as the temperature increases, the spin flop is slightly suppressed until disappearing completely at temperatures higher than Néel temperature as presented in the inset of **Figure 6(f)**. On the other hand, no spin flop transitions appeared in case of $\mathbf{H} \parallel \mathbf{ab}$ (**Figure 6(g)**) for the pristine CuCrP_2S_6 as well as for the doped compound $\text{CuCrP}_2\text{S}_{4.8}\text{Se}_{1.2}$ in both $\mathbf{H} \perp \mathbf{ab}$ (**Figure 6(h)**) and $\mathbf{H} \parallel \mathbf{ab}$ (**Figure 6(i)**). According to the linear profile between \mathbf{M} and \mathbf{H} for CuCrP_2S_6 ($X=0$) and $\text{CuCrP}_2\text{S}_{4.8}\text{Se}_{1.2}$ ($X=0.2$) for both $\mathbf{H} \perp \mathbf{ab}$ and $\mathbf{H} \parallel \mathbf{ab}$ states at different temperatures, the magnetic susceptibility is almost the same for the temperatures lower than Néel temperature ($T=1.8$ K, $T=5$ K, and $T=10$ K) while it is largely changed for the temperatures higher than Néel temperature ($T=50$ K and $T=100$ K). It is seen that with increasing the temperature, the magnetic susceptibility for CuCrP_2S_6 ($X=0$) and $\text{CuCrP}_2\text{S}_{4.8}\text{Se}_{1.2}$ ($X=0.2$) decreases independently on the crystallographic directions. In addition, the magnetic susceptibility of the pure CuCrP_2S_6 ($X=0$) structures is higher than that for the doped $\text{CuCrP}_2\text{S}_{4.8}\text{Se}_{1.2}$ ($X=0.2$) structure. By comparing the temperature variation effects with the effects of the doping amount change on the spin flop transitions, it is found that the change in the selenium doping amount can suppress these transitions larger than the suppression resulting from the change in the temperature. This confirms that the variations in selenium dopants are more efficient in modulating the spin flop transition than the temperature variations.

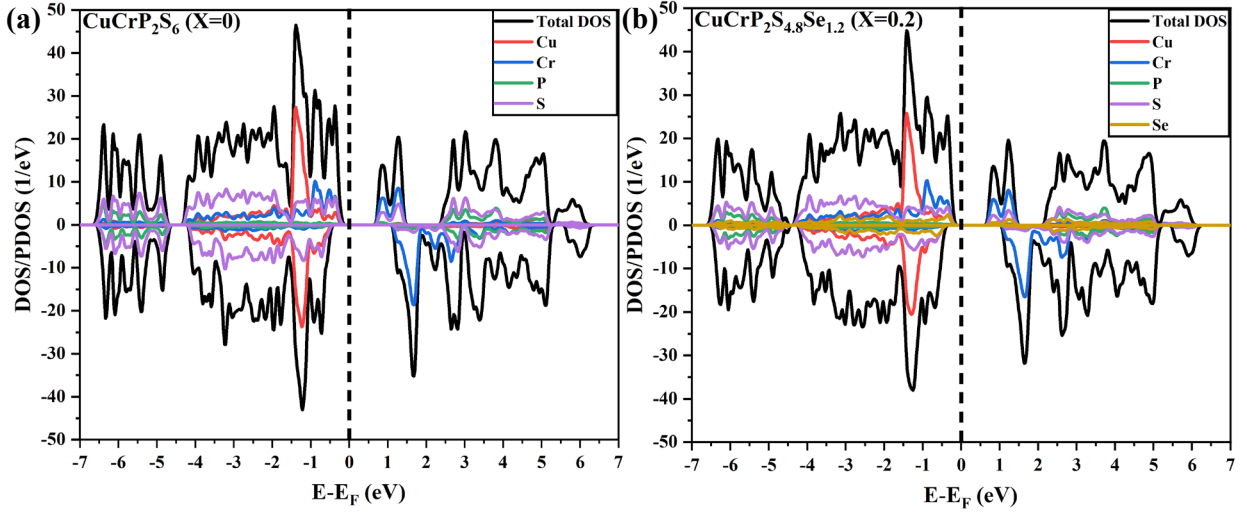


Figure 7: Total and projected density of states of **(a)** CuCrP_2S_6 and **(b)** Se-doped CuCrP_2S_6 ($\text{CuCrP}_2\text{S}_{4.8}\text{Se}_{1.2}$)

Total density of states (TDOS) and projected density of states (PDOS) of each element in **Figure 7** show the asymmetric characteristics between spin-up and spin-down states in both parent (**Figure 7(a)**) and doped (**Figure 7(b)**) systems. As shown in **Figure 7(a)**, the contribution of S is dominant at -0.16 eV (top of the valence band) while the contribution of Cr becomes more dominant after Se doping at the same energy value as shown in **Figure 7(b)**. In addition, Cr has the pronounced contribution at the bottom of the conduction bands for the pristine and doped compounds at 0.67 eV and 0.66 eV, respectively. On the left-hand side (LHS) of **Figures 7(a)** and **7(b)**, the hybridization of spin-up states of Cr is the strongest, ranging from -0.46 eV to -0.93 eV for the undoped crystal and from -0.33 eV to -0.99 eV for the doped one. On the other hand, the hybridization of spin-up and spin-down states of Cr in the right-hand side (RHS) becomes very strong in the energy range from 0.75 eV to 2.34 eV for the pristine structure and from 0.7 eV to 2.1 eV for the doped one. Also, the contribution of Cu is the largest and more efficient only during the energy ranges from -1.1 eV to -1.5 eV for CuCrP_2S_6 (**Figure 7(a)**) and from -1 eV to -1.53 eV for $\text{CuCrP}_2\text{S}_{4.8}\text{Se}_{1.2}$ (**Figure 7(b)**). Besides, in doped compound (**Figure 7(b)**), the contribution of P's spin-up states is only observed in its dominant form in the energy interval ranged from 3.6 eV to 3.8 eV while S's contribution becomes evidently dominant at the same energy interval in the undoped compound (**Figure 7(a)**). The S's hybridization has a great effect compared to other hybridizations in both parent (from -1.6 eV to -6.5 eV in LHS and from 2.95 eV to 6.2 eV in RHS) and doped (-1.9 eV to -6.5 eV in LHS and 2.8 eV to 3.5 eV in RHS) structures. Moreover, the hybridization intensity of S contributions in LHS of **Figures 7(a)** and **(b)** is higher than that in RHS for both undoped and doped systems. Notably, the hybridization intensity of Se contributions is weaker than all hybridizations in the doped compound. In general, the hybridization intensities in parent structure decrease largely under Se addition due to strong orbital interactions between Se atoms and its neighbors. Finally, it is confirmed that the Se doping can greatly modify the asymmetric behavior of spin-up and spin-down states which has an effective role in the anisotropy in the pristine CuCrP_2S_6 crystals.

IV. Conclusions

In summary, chemical vapor transport technique was used to synthesize high quality crystals of $\text{CuCrP}_2(\text{S}_{1-x}\text{Se}_x)_6$ (where $X=0, 0.02, 0.05, 0.1,$ and 0.2). These crystals were characterized by SEM, EDS, XRD, HRTEM, SAED and XPS. The magnetic measurements were carried out in perpendicular and parallel directions between the external magnetic field (\mathbf{H}) and the crystallographic plane (\mathbf{ab}). In addition, spin polarized DFT calculations were performed to study the effect of selenium substitution on the magnetic properties of the pure CuCrP_2S_6 . The experimental results revealed that magnetic anisotropy can be greatly controlled, especially in the antiferromagnetic phase, via selenium doping. Besides, T_N values decrease with increasing the selenium concentrations. T_{Max} for $\mathbf{H} \parallel \mathbf{ab}$ is higher than that for $\mathbf{H} \perp \mathbf{ab}$ except at $X=0.05$ where they have the same values. In both $\mathbf{H} \parallel \mathbf{ab}$ and $\mathbf{H} \perp \mathbf{ab}$ cases, T_{Max} values decrease with increasing the selenium concentrations. The suppressions of spin flop transitions, which appear only in case of $\mathbf{H} \perp \mathbf{ab}$, can be tuned predominantly due to the increase in selenium concentrations and slightly due to the increase in the temperature. The transitions of spin flop appeared only at $T < T_N$ (antiferromagnetic phase) while they disappeared at $T > T_N$ (paramagnetic phase). Also, the appearance of these transitions occurred only at $X=0, 0.02, 0.05$ while their disappearance was observed at $X = 0.1, 0.2$. DFT calculations confirmed that selenium doping in CuCrP_2S_6 has a high contribution to change the asymmetric characteristics between spin up and spin down states. It is evident that the tunable magnetic anisotropy in this material makes it a suitable candidate for spintronic devices applications.

V. Author Contributions

I. S. E. set up the experimental design, material synthesis, data analysis, computational calculations and writing the original draft of the manuscript; L. S. contributed in conceptualization, supervision and manuscript review & editing.

VI. Acknowledgements

We would like to express our thanks to Dr. Zia ur Rehman (Visiting Researcher at National Synchrotron Radiation Laboratory, University of Science and Technology of China, Hefei, Anhui 230029, China) and Dr. Ahmed Shahboub (Postdoctoral Researcher at Hefei Institutes of Physical Sciences, Chinese Academy of Sciences, Hefei, China) for their fruitful discussions.

References:

- [1] Duong, D. L., Yun, S. J., & Lee, Y. H. (2017). van der Waals layered materials: opportunities and challenges. *ACS nano*, 11(12), 11803-11830.
- [2] Sierra, J. F., Fabian, J., Kawakami, R. K., Roche, S., & Valenzuela, S. O. (2021). Van der Waals heterostructures for spintronics and opto-spintronics. *Nature Nanotechnology*, 16(8), 856-868.
- [3] Zhu, J., Yang, Y., Jia, R., Liang, Z., Zhu, W., Rehman, Z. U., ... & Huang, R. (2018). Ion gated synaptic transistors based on 2D van der Waals crystals with tunable diffusive dynamics. *Advanced Materials*, 30(21), 1800195.

- [4] Rao, T., Wang, H., Zeng, Y. J., Guo, Z., Zhang, H., & Liao, W. (2021). Phase transitions and water splitting applications of 2D transition metal dichalcogenides and metal phosphorous trichalcogenides. *Advanced Science*, 8(10), 2002284.
- [5] Gusmão, R., Sofer, Z., Sedmidubsky, D., Huber, S., & Pumera, M. (2017). The role of the metal element in layered metal phosphorus triselenides upon their electrochemical sensing and energy applications. *ACS Catalysis*, 7(12), 8159-8170.
- [6] Oliveira, F. M., Paštika, J., Pires, L. S., Sofer, Z., & Gusmao, R. (2021). Photoelectrochemical Activity of Layered Metal Phosphorous Trichalcogenides for Water Oxidation. *Advanced Materials Interfaces*, 8(11), 2100294.
- [7] Gusmão, R., Sofer, Z., & Pumera, M. (2019). Metal phosphorous trichalcogenides (MPCh₃): from synthesis to contemporary energy challenges. *Angewandte Chemie International Edition*, 58(28), 9326-9337.
- [8] Cheng, Z., Sendeku, M. G., & Liu, Q. (2020). Layered metal phosphorous trichalcogenides nanosheets: facile synthesis and photocatalytic hydrogen evolution. *Nanotechnology*, 31(13), 135405.
- [9] Chittari, B. L., Park, Y., Lee, D., Han, M., MacDonald, A. H., Hwang, E., & Jung, J. (2016). Electronic and magnetic properties of single-layer MPX₃ metal phosphorous trichalcogenides. *Physical Review B*, 94(18), 184428.
- [10] Brec, R. (1986). Review on structural and chemical properties of transition metal phosphorous trisulfides MPS₃. *Solid State Ionics*, 22(1), 3-30.
- [11] Wang, F., Shifa, T. A., Yu, P., He, P., Liu, Y., Wang, F., ... & He, J. (2018). New frontiers on van der Waals layered metal phosphorous trichalcogenides. *Advanced Functional Materials*, 28(37), 1802151.
- [12] Ouvrard, G., Brec, R., & Rouxel, J. (1985). Structural determination of some MPS₃ layered phases (M= Mn, Fe, Co, Ni and Cd). *Materials research bulletin*, 20(10), 1181-1189.
- [13] Park, C. B., Shahee, A., Kim, K. T., Patil, D. R., Guda, S. A., Ter-Oganessian, N., & Kim, K. H. (2022). Observation of spin-induced ferroelectricity in a layered van der Waals antiferromagnet CuCrP₂S₆. *Advanced Electronic Materials*, 8(6), 2101072.
- [14] Cho, K., Lee, S., Kalaivanan, R., Sankar, R., Choi, K. Y., & Park, S. (2022). Tunable ferroelectricity in van der Waals layered antiferroelectric CuCrP₂S₆. *Advanced Functional Materials*, 32(36), 2204214.
- [15] Ma, Y., Yan, Y., Luo, L., Pazos, S., Zhang, C., Lv, X., ... & Zhang, X. (2023). High-performance van der Waals antiferroelectric CuCrP₂S₆-based memristors. *Nature Communications*, 14(1), 7891.
- [16] Cajipea, V. B., Ravez, J., Maisonneuve, V., Simon, A., Payen, C., Von Der Muhll, R., & Fischer, J. E. (1996). Copper ordering in lamellar CuMP₂S₆ (M= Cr, In): transition to an antiferroelectric or ferroelectric phase. *Ferroelectrics*, 185(1), 135-138.
- [17] Susner, M. A., Rao, R., Pelton, A. T., McLeod, M. V., & Maruyama, B. (2020). Temperature-dependent Raman scattering and x-ray diffraction study of phase transitions in layered multiferroic CuCrP₂S₆. *Physical Review Materials*, 4(10), 104003.
- [18] Colombet, P., Leblanc, A., Danot, M., & Rouxel, J. (1982). Structural aspects and magnetic properties of the lamellar compound Cu_{0.50}Cr_{0.50}PS₃. *Journal of Solid State Chemistry*, 41(2), 174-184.
- [19] Selter, S., Bestha, K. K., Bhattacharyya, P., Özer, B., Shemerliuk, Y., Roslova, M., ... & Aswartham, S. (2023). Crystal growth, exfoliation, and magnetic properties of quaternary quasi-two-dimensional CuCrP₂S₆. *Physical Review Materials*, 7(3), 033402.

- [20] Wang, X., Shang, Z., Zhang, C., Kang, J., Liu, T., Wang, X., ... & Zhao, J. (2023). Electrical and magnetic anisotropies in van der Waals multiferroic CuCrP2S6. *Nature Communications*, 14(1), 840.
- [21] Shemerliuk, Y., Zhou, Y., Yang, Z., Cao, G., Wolter, A. U., Büchner, B., & Aswartham, S. (2021). Tuning magnetic and transport properties in quasi-2D (Mn_{1-x}Ni_x)₂P₂S₆ single crystals. *Electronic Materials*, 2(3), 284-298.
- [22] Cheng, M., Iyer, A. K., Zhou, X., Tyner, A., Liu, Y., Shehzad, M. A., ... & Dravid, V. P. (2022). Tuning the Structural and Magnetic Properties in Mixed Cation Mn_xCo_{2-x}P₂S₆. *Inorganic chemistry*, 61(35), 13719-13727.
- [23] Ur Rehman, Z., Muhammad, Z., Adetunji Moses, O., Zhu, W., Wu, C., He, Q., ... & Song, L. (2018). Magnetic isotropy/anisotropy in layered metal phosphorous trichalcogenide MPS₃ (M= Mn, Fe) single crystals. *Micromachines*, 9(6), 292.
- [24] Kim, T. Y., & Park, C. H. (2021). Magnetic anisotropy and magnetic ordering of transition-metal phosphorus trisulfides. *Nano Letters*, 21(23), 10114-10121.
- [25] Selter, S., Shemerliuk, Y., Sturza, M. I., Wolter, A. U., Büchner, B., & Aswartham, S. (2021). Crystal growth and anisotropic magnetic properties of quasi-two-dimensional (Fe_{1-x}Ni_x)₂P₂S₆. *Physical Review Materials*, 5(7), 073401.
- [26] Lu, Z., Yang, X., Huang, L., Chen, X., Liu, M., Peng, J., ... & Liu, J. M. (2022). Evolution of magnetic phase in two-dimensional van der Waals Mn_{1-x}Ni_xPS₃ single crystals. *Journal of Physics: Condensed Matter*, 34(35), 354005.
- [27] Abraham, J. J., Senyk, Y., Shemerliuk, Y., Selter, S., Aswartham, S., Büchner, B., ... & Alfonsov, A. (2023). Magnetic anisotropy and low-energy spin dynamics in the van der Waals compounds Mn₂P₂S₆ and MnNiP₂S₆. *Physical Review B*, 107(16), 165141.
- [28] Kleemann, W., Shvartsman, V. V., Borisov, P., Banys, J., & Vysochanskii, Y. M. (2011). Magnetic and polar phases and dynamical clustering in multiferroic layered solid solutions CuCr_{1-x}In_xP₂S₆. *Physical Review B—Condensed Matter and Materials Physics*, 84(9), 094411.
- [29] Basnet, R., Kotur, K. M., Rybak, M., Stephenson, C., Bishop, S., Autieri, C., ... & Hu, J. (2022). Controlling magnetic exchange and anisotropy by nonmagnetic ligand substitution in layered MPX₃ (M= Ni, Mn; X= S, Se). *Physical Review Research*, 4(2), 023256.
- [30] Han, H., Lin, H., Gan, W., Liu, Y., Xiao, R., Zhang, L., ... & Li, H. (2023). Emergent mixed antiferromagnetic state in MnPS₃ (1-x)Se_{3x}. *Applied Physics Letters*, 122(3).
- [31] Kresse, G., & Furthmüller, J. (1996). Efficient iterative schemes for ab initio total-energy calculations using a plane-wave basis set. *Physical review B*, 54(16), 11169.
- [32] Perdew, J. P., Burke, K., & Ernzerhof, M. (1996). Generalized gradient approximation made simple. *Physical review letters*, 77(18), 3865.
- [33] Blöchl, P. E. (1994). Projector augmented-wave method. *Physical review B*, 50(24), 17953.
- [34] Kresse, G., & Joubert, D. (1999). From ultrasoft pseudopotentials to the projector augmented-wave method. *Physical review b*, 59(3), 1758.
- [35] Monkhorst, H. J., & Pack, J. D. (1976). Special points for Brillouin-zone integrations. *Physical review B*, 13(12), 5188.
- [36] Binnewies, M., Glaum, R., Schmidt, M., & Schmidt, P. (2012). Chemical vapor transport reactions. *Walter de Gruyter*.
- [37] Io, W. F., Pang, S. Y., Wong, L. W., Zhao, Y., Ding, R., Mao, J., ... & Hao, J. (2023). Direct observation of intrinsic room-temperature ferroelectricity in 2D layered CuCrP₂S₆. *Nature Communications*, 14(1), 7304.

- [38] Lin, B., Chaturvedi, A., Di, J., You, L., Lai, C., Duan, R., ... & Liu, F. (2020). Ferroelectric-field accelerated charge transfer in 2D CuInP2S6 heterostructure for enhanced photocatalytic H₂ evolution. *Nano Energy*, 76, 104972.
- [39] Hu, Y., Li, B., Jiao, X., Zhang, C., Dai, X., & Song, J. (2018). Stable cycling of phosphorus anode for sodium-ion batteries through chemical bonding with sulfurized polyacrylonitrile. *Advanced Functional Materials*, 28(23), 1801010.
- [40] Wang, H., Zhang, M., & Lv, Q. (2019). Removal efficiency and mechanism of Cr (VI) from aqueous solution by maize straw biochars derived at different pyrolysis temperatures. *Water*, 11(4), 781.
- [41] Chen, Y., An, D., Sun, S., Gao, J., & Qian, L. (2018). Reduction and removal of chromium VI in water by powdered activated carbon. *Materials*, 11(2), 269.
- [42] Habib, M., Muhammad, Z., Khan, R., Wu, C., Ur Rehman, Z., Zhou, Y., ... & Song, L. (2018). Ferromagnetism in CVT grown tungsten diselenide single crystals with nickel doping. *Nanotechnology*, 29(11), 115701.
- [43] Muhammad, Z., Li, Y., Ullah, S., Khan, F., Alarfaji, S. S., Alanazi, A. M., ... & Zhao, W. (2024). Extrinsic n-type semiconductor transition in ZrSe₂ with the metallic character through hafnium substitution. *Journal of Alloys and Compounds*, 980, 173616.
- [44] Joy, P. A., & Vasudevan, S. (1992). Magnetism in the layered transition-metal thiophosphates M₂PS₃ (M= Mn, Fe, and Ni). *Physical Review B*, 46(9), 5425.
- [45] Abramchuk, M., Jaszewski, S., Metz, K. R., Osterhoudt, G. B., Wang, Y., Burch, K. S., & Tafti, F. (2018). Controlling magnetic and optical properties of the van der Waals crystal CrCl_{3-x}Br_x via mixed halide chemistry. *Advanced materials*, 30(25), 1801325.
- [46] Zhou, H., Liu, Y., Wang, Z., Guo, Y., Xie, Y., & Wu, C. (2024). Two-dimensional metamagnetism in van der Waals layered material Cu_{2-x}Fe_{1-x}PS₃. *Science China Materials*, 67(2), 658-664.